small methods
www.small-methods.com

Introducing Design Strategies to Preserve N-Heterocycles Throughout the On-Surface Synthesis of Graphene Nanostructures

Maria Tenorio, Cesar Moreno, Manuel Vilas-Varela, Jesús Castro-Esteban, Pol Febrer, Miguel Pruneda, Diego Peña,* and Aitor Mugarza**

Despite the impressive advances in the synthesis of atomically precise graphene nanostructures witnessed during the last decade, advancing in compositional complexity faces major challenges. The concept of introducing the desired functional groups or dopants in the molecular precursor often fails due to their lack of stability during the reaction path. Here, a study on the stability of different pyridine and pyrimidine moieties during the on-surface synthesis of graphene nanoribbons on Au(111) is presented. Combining bond-resolved scanning tunneling microscopy with X-ray photoelectron spectroscopy, the thermal evolution of the nitrogen dopants throughout the whole reaction sequence is tracked. A comparative experimental and ab initio electronic characterization confirms the presence of dopants in the final structures, revealing also that the pyridinic nitrogen leads to a significant band downshift. The results demonstrate that, by using synthetic strategies to lower the reaction temperatures, one can preserve specific N-heterocycles throughout all the reaction steps of the synthesis of graphene nanoribbons and beyond the interibbon coupling reaction that leads to nanoporous graphene.

1. Introduction

Adding nitrogen atoms to the edges and pores of graphene-based nanostructures is an effective strategy to provide a manifold of interesting properties that amplify the potential applications of the undoped counterparts. It implies, among others, the tunability of the electronic properties,[1,2] the generation of metal-free catalysts,[3–8] the complexation with transition metal and lanthanides for single atom catalysts[9,10] and photon emitters,[11] and the affinity enhancement of target species for sensing and filtering,[12–15] as well as of alkaline atoms for energy storage applications.[10,16]

Most of these applications require a control on the density, distribution, and bonding configuration of dopants that is hardly achievable by top-down methods. The latter is particularly critical, since nitrogen dopants can acquire up to eight bonding configurations in graphene nanostructures.[17,18] Indeed, the different methods of post-synthesis addition of nitrogen dopants lead to multiple bonding configurations and their random distribution at irregular edges or pores.[15,19–21]

Bottom-up methods such as the on-surface synthesis (OSS) and the use of specifically designed molecular precursors can offer a solution to simultaneously control both the atomic structure and the chemical composition.[22] The best example is the bottom-up synthesis of graphene nanoribbons (GNRs), where

M. Tenorio[+], C. Moreno, P. Febrer, M. Pruneda, A. Mugarza
Catalan Institute of Nanoscience and Nanotechnology (ICN2)
CSIC and The Barcelona Institute of Science and Technology
Bellaterra, Barcelona 08193, Spain
E-mail: cesar.moreno@unican.es; aitor.mugarza@icn2.cat

The ORCID identification number(s) for the author(s) of this article can be found under https://doi.org/10.1002/smtd.202300768

[+]Present address: IMDEA Nanoscience, Cantoblanco, Madrid 28049, Spain

DOI: 10.1002/smtd.202300768

C. Moreno
Departamento de Ciencias de la Tierra y Física de la Materia Condensada
Universidad de Cantabria
Santander 39005, Spain

M. Vilas-Varela, J. Castro-Esteban, D. Peña
Centro de Investigación en Química Biolóxica e Materiais Moleculares (CiQUS)
Departamento de Química Orgánica
Universidade de Santiago de Compostela
Santiago de Compostela 15782, Spain
E-mail: diego.pena@usc.es

A. Mugarza
ICREA Institució Catalana de Recerca i Estudis Avançats
Barcelona 08010, Spain

several heteroatoms and functional groups have been introduced with the same atomic precision as the rest of the structural parameters.[2,23–33] However, these studies also reflect that, in particular when located at the edges, the functional groups in most cases suffer from isomerization,[33] chemical transformation,[25] or partial[30,31] and even total cleavage[34] during the thermally assisted on-surface synthesis.

Taking into account the aforementioned stability issues, and with the aim of extending the reaction sequence to the synthesis of supraribbon nanostructures, we have carried out a systematic study of the stability of N-heterocycles throughout the on-surface synthesis of graphene nanoribbons and their coupling into nanoporous graphene (NPG). In particular, we have focused on the synthesis of N-doped counterparts of the 7–13 AGNR and the corresponding NPG that can be obtained by using a bisphenyl substituted bianthracene precursor.[35,36] We find that pyridine functionalized precursors are less thermally stable than their pyrimidine counterparts. The reactivity of the former in fact leads to thermally induced polymerization prior to sublimation in ultra-high vacuum (UHV), impeding the deposition of precursors on the surface. In contrast, the less basic pyrimidine groups are thermally stable enough to permit their deposition and withstand all the reaction path up to the synthesis of GNRs. In order to facilitate cross-coupling reactions that could lead to supraribbon structures as the NPG,[35] we introduce a chlorine atom as substituent in the pyrimidine group, with the idea of replacing the dehydrogenative cross-coupling reaction by a Cl-based Ullmann coupling that takes place at lower temperature. The hierarchy between the two Ullmann coupling reactions given by the different C-Br and C-Cl dissociation energies maintain the polymerization and cross-coupling reactions in non-overlapping thermal windows. Our conclusions are founded on a comprehensive scanning tunneling microscopy (STM), X-ray photoelectron spectroscopy (XPS) and density functional theory (DFT) study that correlates structural, chemical and electronic information and provides atomic scale insight into mechanisms that impede or promote the functionalization of graphene nanostructures by OSS.

2. Results and Discussion

Four different N-doped GNR precursors were studied, all bianthracene derivatives substituted in 10,10' positions with bromine atoms and N-heterocycles in 2,2' positions (**Figure 1**), together with their undoped counterpart DP-DBBA (10,10'-dibromo-2,2'-diphenyl-9,9'-bianthracene) parent.[35–37] In monomers **1** and 2, the two phenyl groups at the 2,2' positions of monomer DP-DBBA are replaced by two pyridine rings (4- and 3-pyridinyl, respectively). In monomer 3, the number of N-dopants is increased by replacing the two phenyl substituents in DP-DBBA with two pyrimidines instead (pyrimidin-5-yl). Finally, in monomer 4, we introduce two chloropyrimidine groups in the bianthracene core, in particular two 2-chloropyrimidin-5-yl substituents.

The integrity of the functional groups is already challenged at the first stage of the on-surface synthesis procedure, that is the sublimation of the precursor monomer in ultra-high vacuum (UHV) for its deposition on the catalytic surface. We find that pyridine functionalized monomers 1 and 2 already polymerize before reaching the sublimation temperature, and cannot therefore be deposited on the surface. A MALDI characterization of the material recovered from the evaporator crucible suggests that the unwanted polymerization may be driven by the nucleophilic attack of the pyridine moieties to the electrophilic 10,10' positions of the biantracene core. In contrast, the less basic character of pyrimidines reduces the nucleophilicity of the N lone pairs, preventing the the polymerization of monomers 3 and 4 before sublimation. The stability of the pyrimidine group in these monomers throughout the on-surface synthesis could therefore be studied by tracking the thermal evolution of intermediates and final products, as shown in the following.

Figure 2 summarizes the complementary STM and XPS analysis carried out for each reaction step in order to track the structural and chemical evolution of monomer 3. After its deposition on the Au(111) surface at room temperature, large islands of well-ordered, self-assembled precursor monomers are observed by STM (Figure 2a), denoting a high diffusivity and substantial intermolecular interactions of these molecules on Au(111). Close-up images reveal chain like structures made of protrusion pairs that fit with the staggered conformation of the DBBA core.[36,38] The interlobe lateral distance of 7.4 Å and the apparent height of 2.3 Å indicate that the monomer adsorbs with the pyrimidine groups at the lower side interacting with the Au surface, as found for the phenyl group of the undoped DP-DBBA (see Figure S16, Supporting Information).[36] The superimposed model in the inset of Figure 2a suggests that intrachain interactions are mediated by the pyrimidine groups, whereas Br···H is the dominant interchain interaction.

The integrity of the monomer is confirmed by the XPS results of Figure 2d–f (see SI for more quantitative information on the XPS data analysis). We find that the C 1s core level nicely fits by imposing the stoichiometric relation of bonding components, C-C(H):C-NH:C-Br = 28:6:2. For simplicity, C-C(H), C-NH, C-Br refer respectively to $C[C_2H]/C[C_3]$, $C[CNH]/C[N_2H]$ and $C[C_2Br]$, the former two merging a pair of components into single fitting peaks due to the difficulty to resolve them within our experimental conditions. The binding energies of the components obtained from this fit also agree with that of the pristine molecule. C-C(H) and C-Br lie at 284.3 eV and 284.8 eV, respectively, very close to values obtained for the undoped molecule adsorbed on Au(111),[36] and the value of 285.4 eV obtained for C-NH is characteristic of pyridine groups.[39,40] The Br 3d doublet appears at 70.7/69.7 eV, energies corresponding to C-bonded Br[36,41] For N, we find a single 1s component at 398.8 eV, energy expected for pyridinic N,[17] with relative area close to the stoichiometric relation. Altogether they represent signatures of the pristine molecule.

After postannealing to 150°C, monomers polymerize into 1D chains, as can be seen in the STM images of Figure 2b. One can attribute the polymerization to the Ullmann coupling of monomers by using the complementary information obtained from the XPS analysis: the 2.1 eV upshift of the Br 3d doublet is a clear indicative of cleaved, Au-bonded Br (Figure 2e).[36] This is in agreement with the better fit, we obtain when we turn C-Br bonds into C-C by fixing the C 1s multicomponent relation to C-C(H):C-NH = 30:6 (Figure 2d).

The morphology and distribution of the polymer chains are in stark contrast to that of their undoped counterparts (i.e.,

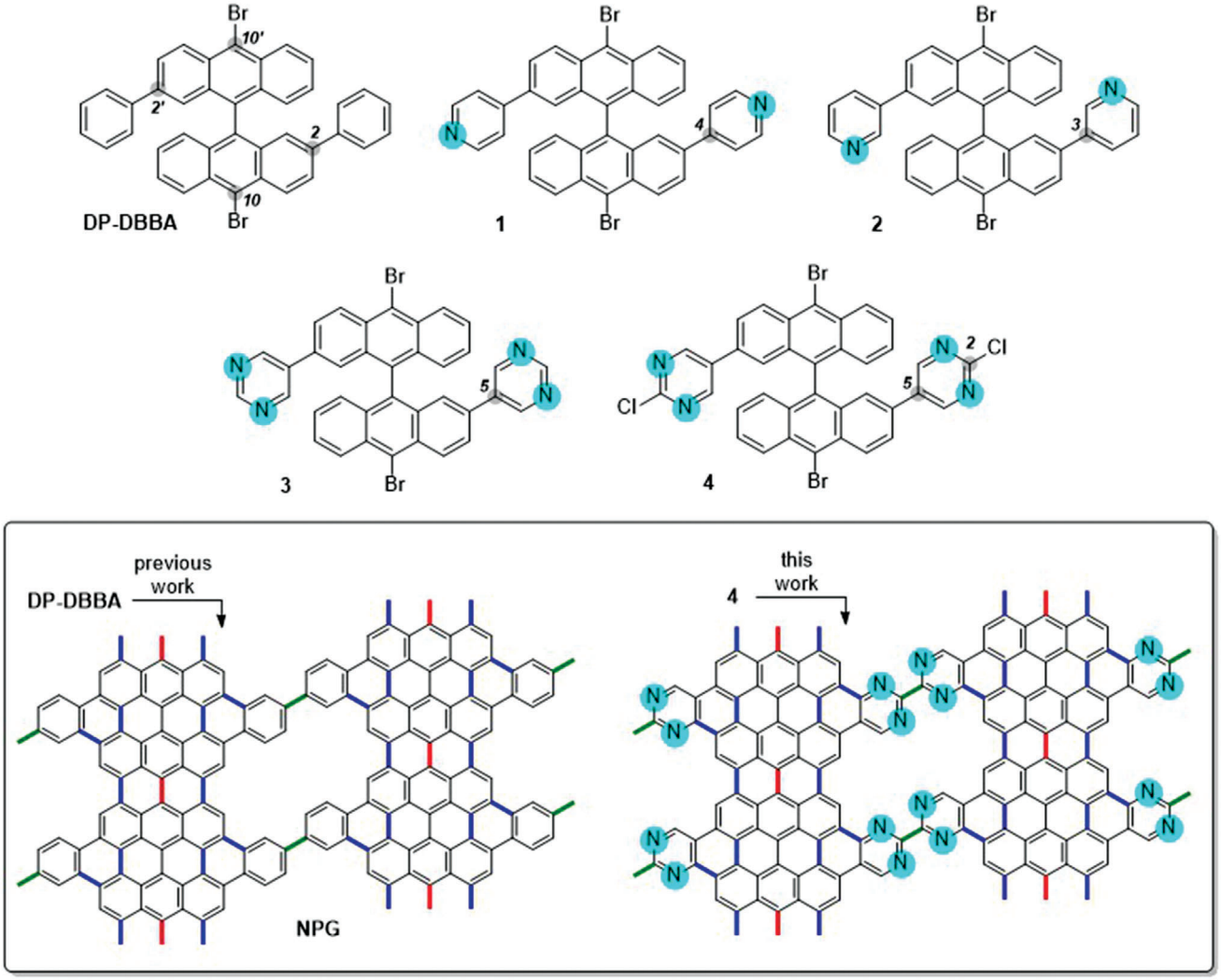

Figure 1. Schematic representation of DP-DBBA, studied in Refs. [35–37], dipyridine derivatives 1 and 2, and dipyrimidine derivatives 3 and 4. The final structures achieved with DP-DBBA in a previous work,[35] and with monomer 4 in this work, are sketched at the bottom. In red, bonds formed by Br-based Ullmann couplings; in blue, bonds formed by cyclodehydrogenations; in green, interibbon Cl-based Ullmann couplings.

DP-DBBA). The pinning of the latter at the elbow dislocations of the herringbone leads to chains with an average length of 70 nm aligned to the zigzag direction of the herringbone reconstruction.[37] Conversely, the N-doped polymers appear mostly confined within the fcc/hcp tracks of the reconstruction, with an average length of 18 ± 8 nm (with a total sample of 78 polymers measured), very close to the characteristic length of the fcc/hcp segments of the zigzag pattern. These differences suggest that N-doped polymers interact more strongly with the Au surface, and as consequence their length is limited rather than guided by the reconstruction pattern, similar to that found for other GNRs.[31]

After further postannealing to 300°C polymer chains, characterized by staggered protrusions in the STM images, appear now as planar structures, with an apparent height of 2.2 Å and the triple bay edge structure that characterize the 7–13 AGNRs (see Figure 2c).[35] The formation of GNRs at 100°C lower temperature as compared to the undoped counterpart denotes that the pyrimidine group (directly or indirectly) promotes the cyclodehydrogenative cyclization of the polymer chain. Although this reaction cannot be directly tracked in the evolution of the XPS spectra due to the proximity of the C-H and C-C components of the C 1s core level, the presence of the residual H can be inferred from the absence of the Br core level, which in many other studies has been attributed to the desorption of HBr.[36,42,43] The survival of the pyrimidine groups to this reaction step is supported by the fact that the N 1s peak remains at the same energy and relative area (Figure 2f), although the twofold increase in width already indicates the onset of some transformations, as it will be discussed later.

The presence of the N-dopants at the *cata*-fused pheripheral rings as well as their site distribution can be explored in detail by a comparative analysis of bond-resolved (BR)-STM images. The example displayed in **Figure 3**a shows clear contrast differences between the edge rings of undoped and N-doped GNRs. Those of the N-doped GNRs appear with lower contrast, as has

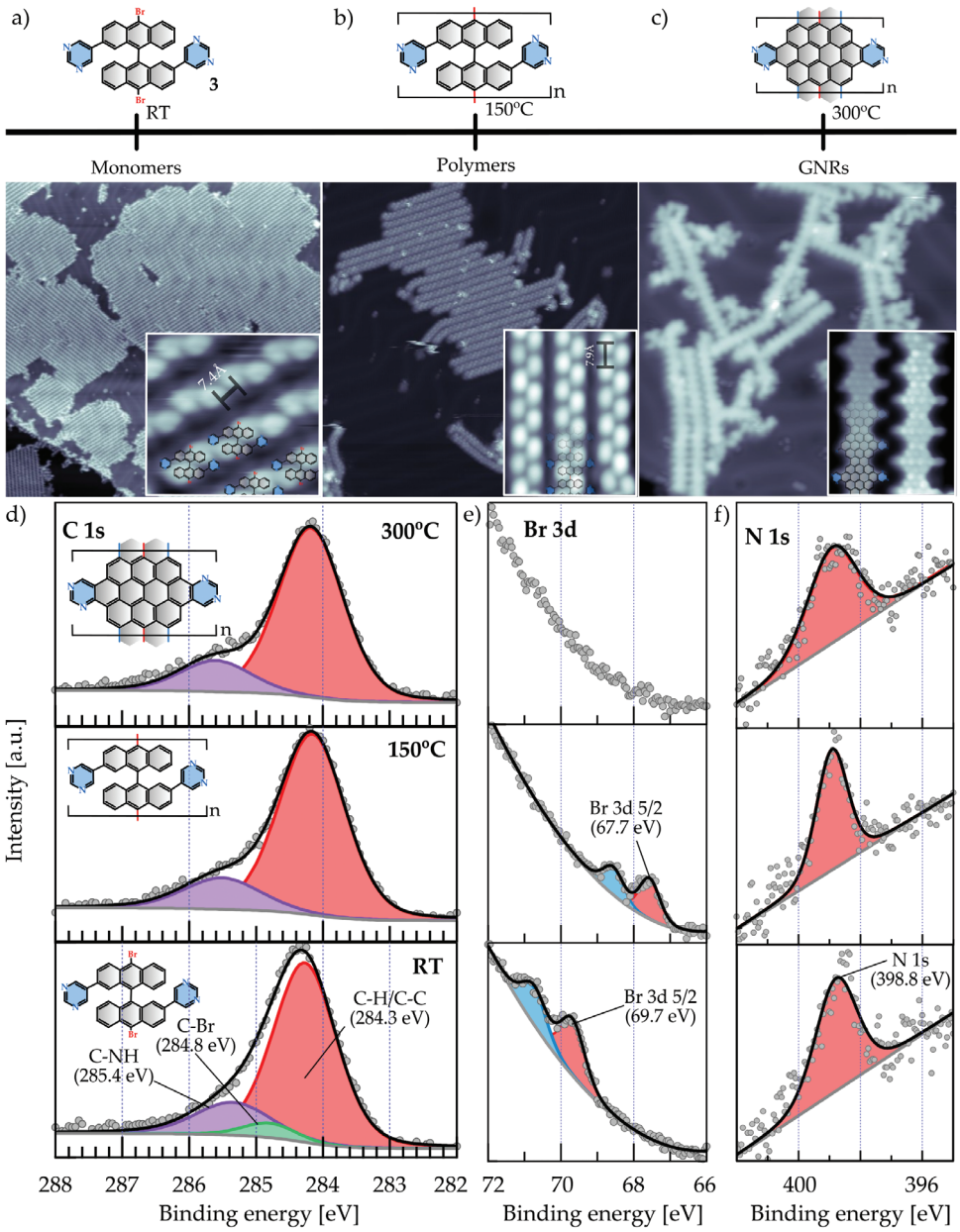

Figure 2. On-surface synthesis of edge nitrogen-doped graphene nanoribbons from monomer 3, and characterization of electronic properties. a–c) STM images (overview and representative closeview) of the stepwise reaction to grow edge nitrogen-doped graphene nanoribbons. From left to right: as-deposited monomers, 1D polymers, and graphene nanoribbons. d–f) XPS analysis of the C 1s (d), Br 3d (e), and N 1s (f) core levels for monomer 3 at different temperatures of postannealing. STM parameters are listed in Table S8 (Supporting Information).

been observed for other N-heterocycle containing structures.[26,45] A more detailed anaylsis of the appearance of edge rings in the N-doped GNRs reveals asymmetric features that are inverted at opposing edges. The asymmetry mimics that imprinted by the nitrogen heteroatoms to a fused pyrimidine ring, which is a robust evidence of their integrity. Their homogeneous distribution along each edge of the ribbon, on the other hand, is a direct proof of the formation of homochiral GNRs, which is a crucial ingredient for the interibbon interaction and the potential formation of nanoporous graphene by their lateral coupling, as pictured in Figure 3b.

Similar to the case of polymers, the presence of N-dopants at the edges seems to determine the GNR distribution on the surface. Instead of evenly dispersed by the interaction with the reconstructed Au surface as observed for the undoped GNRs,[37] N-doped GNRs appear bundled, suggesting dominating attractive interibbon interactions. By superimposing models to an interacting pair of GNRs, as done in Figure 3b, we conclude that the attractive interaction is driven by an effective N ⋯ H pairing between pyrimidines (4 N⋯H pairs per pyrimidine). Such N⋯H interaction configuration can only be found between pyrimidines of homochiral pairs of GNRs, which in turn is the configuration

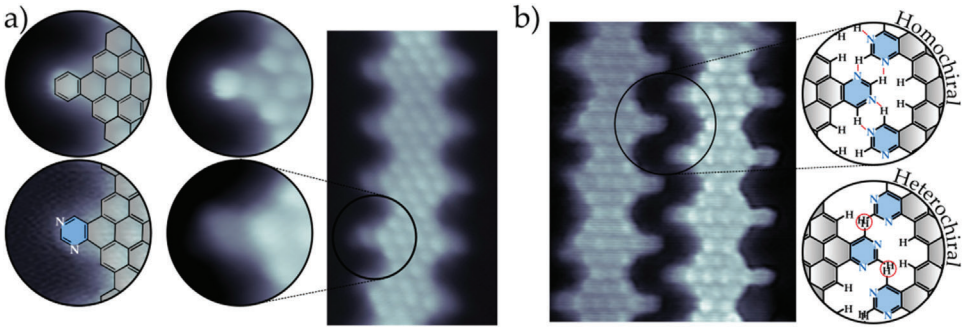

Figure 3. Identification of nitrogen atoms in pyrimidine functional groups. a) BR-STM image of a single N-doped GNR, with a zoom in one the outer pyrimidine rings, and the undoped phenyl counterpart. Schemes of the outer aromatic rings have been overlapped for the identification of nitrogen atoms. b) BR-STM image of a couple of interacting N-doped GNRs, with structural models that would correspond to homochiral and heterochiral pairs, showing that only the former would lead to stable bonding configuration. STM parameters are listed in Table S8 (Supporting Information).

that would lead to the energetically favorable covalent bonding in the formation of NPG. By tracing back chirality at each step of the formation of GNRs, we note that the homochiral distributions of interacting GNRs are enabled by the fact that enantiopure interactions determine the assembly of both monomer and polymer intermediates. The homochiral polymer ensemble shown in Figure 2b is one example of it, as can be inferred from the same staggering sequence derived from the lobes.

The charge accumulation induced by the higher electron affinity of pyridinic nitrogen dopants at the edge of GNRs are expected to inductively downshift the frontier electronic bands,[2,46,47] thus spectroscopic measurements represent a further evidence of their presence. Indeed, the comparative dI/dV spectra acquired at the undoped and N-doped GNRs displayed in **Figure 4**a exhibit a downshift of the valence band maximum (VBM) and conduction band minimun (CBM) of 0.3 and 0.2 eV respectively, with a minor increase in the gap from 1.25 to 1.35 eV. The identification of the VBM and CBM is supported by the comparison of constant height dI/dV maps with the corresponding wave functions, as obtained from our ab initio calculations, both showing the same nodal symmetry (Figure 4b, see Section S1.4, Supporting Information for more details in the band identification). Accordingly, the band structures obtained in the same calculations reproduce the rigid downshift induced by the N heteroatoms (see Figure S17, Supporting Information for equivalent calculations on the corresponding NPG structures). The slightly larger value of 0.54 eV, we obtain for the shift can be explained by the absence of the substrate in the calculations, which can partially screen the inductive shift observed experimentally. The equivalent DFT calculations carried out for the corresponding NPG structures

The homochiral interibbon N···H interaction configuration of Figure 3b represents an ideal preconformation for the dehydrogenative C-C cross-coupling required for the lateral bonding of the GNRs into a N-doped NPG, in analogy to that leading to the undoped NPG.[35] To test this final reaction step, we gradually increase the postannealing temperature above the 300°C required for the formation of GNRs. For the temperature range between 300–350°C, BR-STM images reveal how the pyrimidine groups start to degrade by following a ring opening reaction that, at the temperature of 400°C, end with a major cleavage (see Figure S18, Supporting Information for a more detailed description of the proposed degradation path). This degradation resembles that previously described for tetrathienoanthracene derivatives.[48] The gradual degradation of pyrimidine groups is in agreement with the XPS data, where the main variation of the N 1s core level peak in the 300–350°C range is an increase in the width that could account for the different N environments, and at 400°C the peak undergoes a significant reduction of around 30–40% of its area (**Figure 5**b).

The degradation of pyrimidine groups at the temperature range expected for the dehydrogenative interibbon coupling inhibits the formation of N-doped NPG by using monomer 3. In order to facilitate the lateral coupling at lower temperatures and preserve the integrity of pyrimidine rings, we have rationally designed monomer 4, already introduced in Figure 1. The new molecular precursor contains chlorine atoms at position 2 of the pyrimidine rings, which is otherwise hydrogenated in monomer 3. The presence of chlorine is expected to decrease the temperature of interibbon coupling by replacing the dehydrogenative path with a second Ullmann coupling reaction. However, we note that, when reducing the cross-coupling temperature, care has to be take on avoiding thermal overlap with other processes such as the intraribbon cyclodehydrogenation, in order to keep a selective, sequential reaction path and avoid ill-defined structures.[49,50]

When deposited at room temperature, monomer 4 behaves similar to 3, forming large, ordered islands driven by intermolecular halogen···H and N···H interactions (**Figure 6**e). It also maintains the same staggered conformation, with the lateral distance between brightest lobes of 7.4 Å. The only distinct characteristic at this stage of the reaction is the increase of the apparent height to 2.9 Å (as compared to 2.3 Å found for 3), which we attribute to the presence of the chlorine atoms at position 2 of the pyrimidine rings (see Figure S16, Supporting Information).

At 100°C of postannealing, the homolythic cleavage of the C-Br starts to take place, and finalizes before 140°C, as indicated by the thermal evolution of the Br 3d peak (Figure 6b). During this reaction step, the chlorinated pyrimidine rings do not seem to be affected, according to the close to stoichiometric C:Cl:N core level relation. We note that in the C 1s core level, a new peak related to the C-Cl ($C[C_2Cl]$) component appears at the highest binding energy tail at 286.9 eV, in agreement with that found for other chlorinated adsorbates.[51]

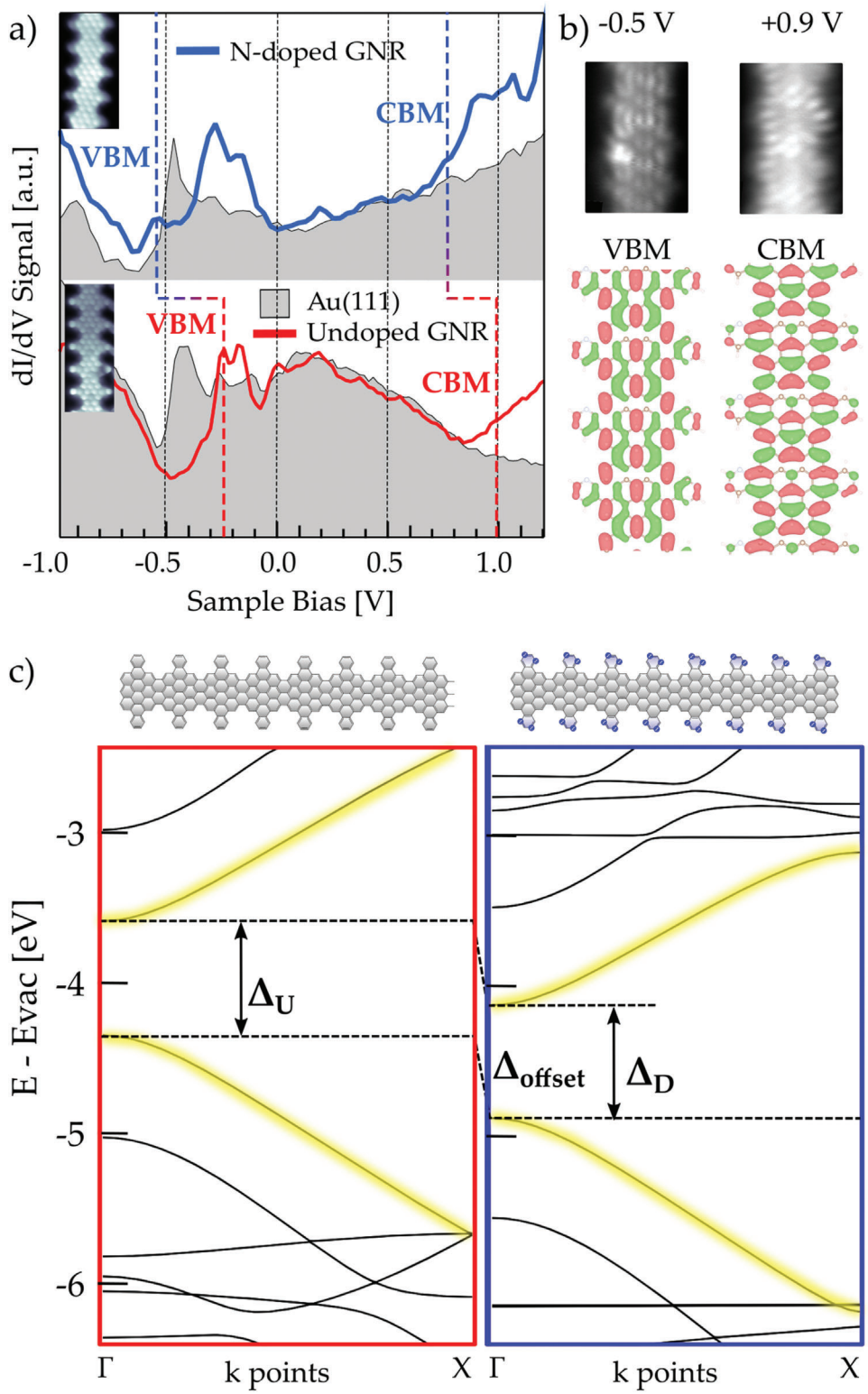

Figure 4. a) dI/dV spectra on undoped (red plot) and nitrogen-doped (blue plot) graphene nanoribbons with their respective bond-resolved STM images. The spectra is acquired at the edge of the bay region, where the wavefunction overlap with the tip is maximized.[35,44] b) Constant height dI/dV maps acquired at -0.5 and 0.9 V at the edge of a nitrogen-doped graphene nanoribbon (top), and the respective VBM and CBM wavefunctions obtained by DFT (bottom). STM parameters of the spectroscopic images are listed in Table S8 (Supporting Information). c) DFT calculations of the band structure of undoped and nitrogen-doped graphene nanoribbons, The frontier bands are highlighted by yellow lines, and the bandgap and the rigid band offset induced by nitrogen heteroatoms are indicated with dashed lines.

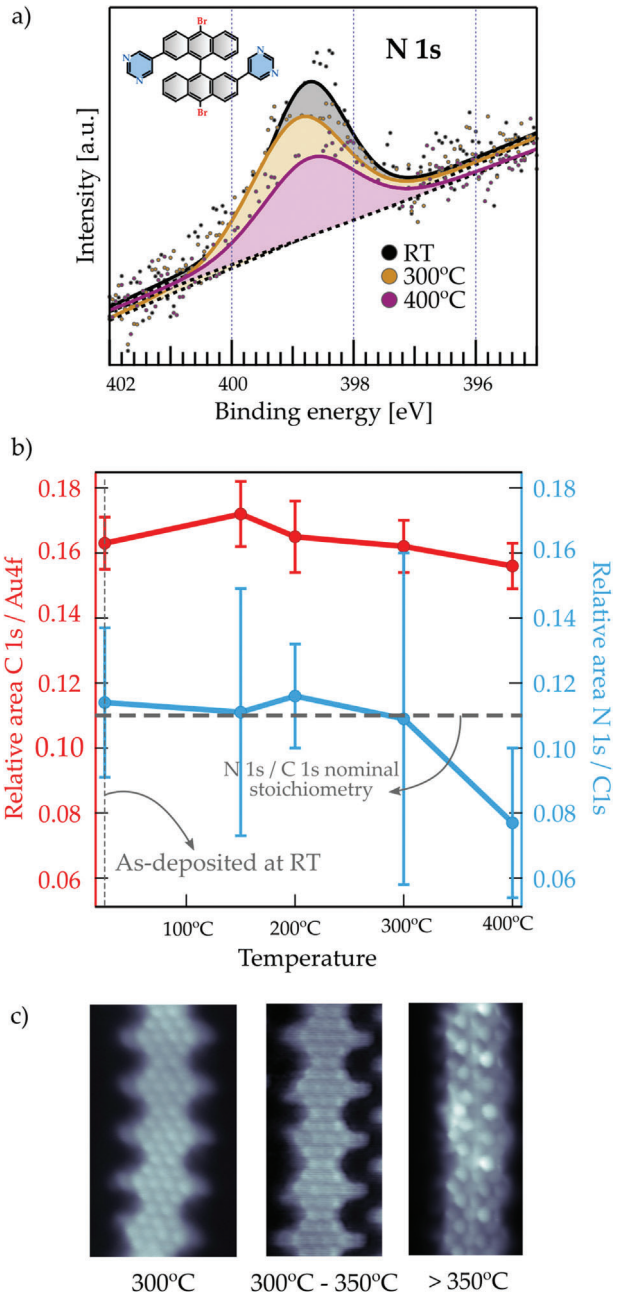

Figure 5. Tracking N 1s XPS core level signal during the OSS reactions of monomer 3. a) N 1s core level peaks at RT (black), 300°C (yellow) and 400°C (purple). Fitting characteristics are listed in Supporting Information. b) Relative area between the corrected signal of the N 1s peak versus the C 1s peak (blue plot) and between the corrected signal of the C 1s peak and the Au 4f doublet peaks. The nominal stoichiometric value has been indicated with a grey dashed line. c) BR-STM images of GNRs postannealed at 300°C–350°C (left image) and at temperatures higher than 350°C (right image). STM parameters are listed in Table S8 (Supporting Information).

The debromination step tracked by XPS is consistent with the Ullmann polymerization observed by STM at 150°C. Similar to that found for monomer 3, the large monomer islands rearrange at this temperature into small polymer bunches. There are, however, substantial differences in the morphology and distribution of the two type of polymers. For poly-4, instead of linear chains coexisting in both fcc and hcp tracks of the Au herringbone reconstruction, we find smaller clusters of meandering polymer chains only in fcc regions of a distorted surface reconstruction (see Figure S19, Supporting Information). The preference to fcc regions,[52] and the removal of the reconstruction induced by the strong interaction with the surface,[53] have both been reported for alkali adsorbates. A similar chlorine-induced redistribution of the herringbone reconstruction has also been observed for another chlorinated graphene nanoribbon.[54] We therefore can conclude that the inclusion of a chlorine atom at the pyrimidine rings set interactions that have profound effects on the morphology and distribution of the corresponding GNRs.

After annealing to 300°C, the absence of Br and Cl core levels indicates that both dechlorination and cyclodehydrogenation have occurred. The former is supported by the fact that the C 1s multiplet can be fitted by discarding the C-Cl component. The latter is, on the other hand, inferred from the fact that halogen desorption in these on-surface synthesis processes is prompted by hydrogenation with the residual hydrogen released in reactions such as the cyclodehydrogenation.[42,55]

The planarization of polymer chains induced by the cyclodehydrogenation is directly visualized by STM, as can be seen in Figure 6g. The analysis of STM images also reveals that the lack of order and formation of non-selective covalent bonds that inhibit the formation of the long-range ordered arrays of laterally fused GNRs that are needed for the realization of NPG. Similar non-selective coupling reactions have also led to irregular structures in the synthesis of armchair ribbons.[49] However, close-up BR-STM images of the series of aligned ribbon pairs that a randomly found on the surface reveal their lateral coupling. This observation proofs that, if the GNRs are prealigned, the hierarchical (C-Br vs C-Cl) Ullmann strategy can be selective enough to form a nanoporous graphene structure by the formation of GNRs and their lateral coupling. It is also a direct demonstration that the reduction of 100–150°C of the cross-coupling temperature achieved by replacing the dehydrogenative path by a second Ullmann coupling reaction can effectively prevent the degradation of the pyrimidine side groups throughout all the reaction sequence needed for the formation of a N-doped NPG.

3. Conclusion

In summary, we have systematically studied thermally induced on-surface synthetic routes to grow N-doped graphene nanoribbons and nanoporous graphene, the latter by the lateral coupling of ribbons. Particular focus has been dedicated to two aspects: i) the effect of the position and number of nitrogen heteroatoms in the functional groups on the thermal stability of the precursor and intermediates; ii) the search for reaction paths that preserve the functional groups throughout the whole process by lowering the onset temperature for the cyclodehydrogenation and interibbon coupling steps that lead correspondingly to the formation of GNRs and their lateral coupling into NPG.

Regarding the first point, we have found that pyrimidine groups are more stable than pyridine substituents in this OSS transformation. The reactivity of pyridine functionalized precursors leads to premature unwanted polymerization prior to sublimation, inhibiting their deposition by thermal evaporation.

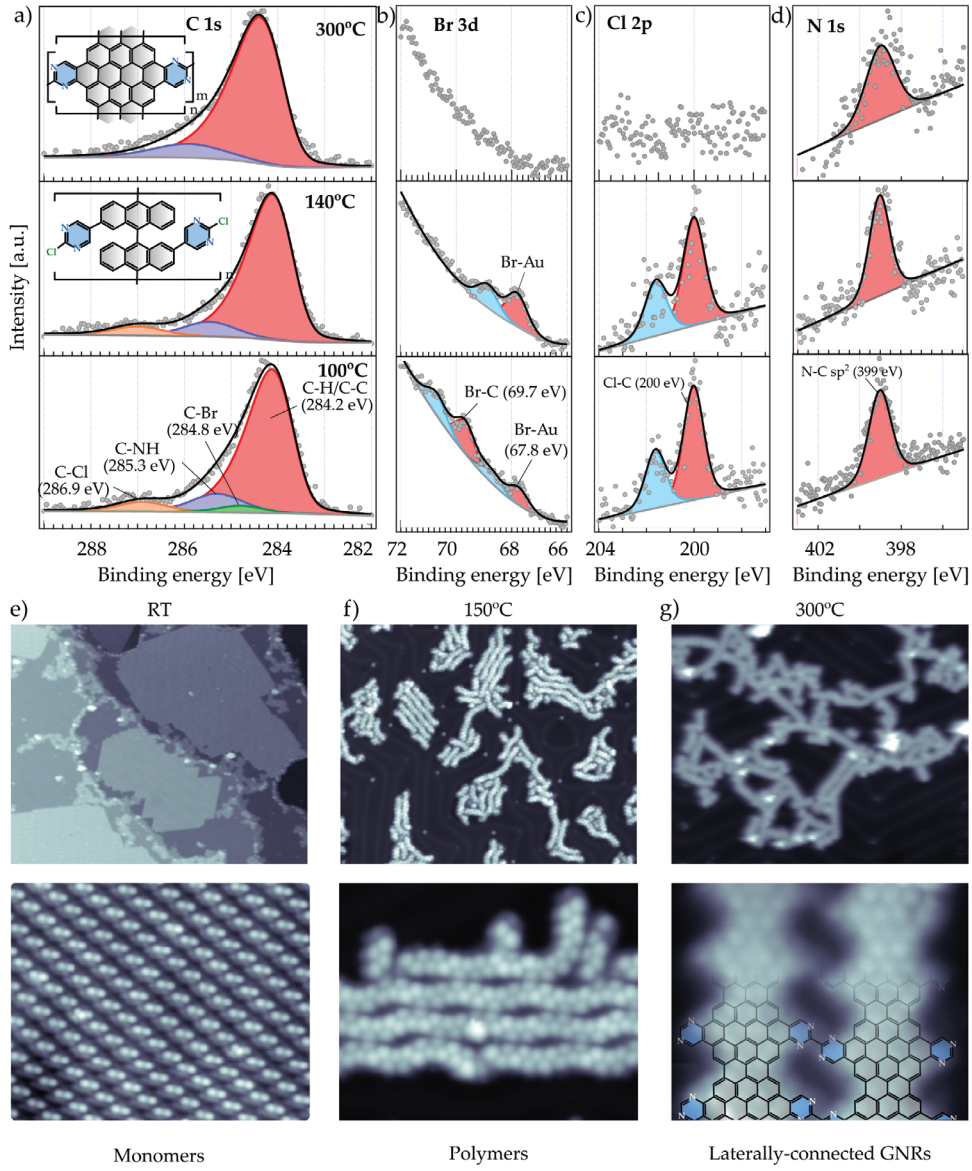

Figure 6. On-surface synthesis of laterally connected edge nitrogen-doped graphene nanoribbons obtained from monomer 4. a–d) XPS spectra of C 1s, Br 3d, Cl 2p, and N 1s at different temperatures of postannealing. e–h) Large scale (top) and closeview (bottom) STM images of the on-surface synthesis of the laterally connected nitrogen doped graphene nanoribbons. e) Self-assembled islands of as-deposited molecules. f) Representative bunches of 1D polymers after postannealing to 150°C. g) Planarized and laterally connected ribbons after postannealing at 300°C. STM parameters are listed in Table S8 (Supporting Information).

In contrast, the pyrimidine functionalized precursors are stable enough for sublimation and withstand all reaction steps up to the formation of GNRs, but degrade before their lateral fusion by dehydrogenative coupling. The temperature of this last step is reduced by 100–150°C as compared to the dehydrogenative cross-coupling of the undoped GNR counterparts by the introduction of chlorine atoms at position 2 of the pyrimidine moieties, thus replacing the dehydrogenative path by a second Ullmann coupling reaction. We find that, when GNRs are properly aligned, the interribbon Ullmann cross-coupling can be induced selectively at temperatures where the pyrimidine group is preserved. We thereby demonstrate that pyrimidine groups withstand all the reaction sequence up to the formation of laterally coupled GNRs. However, the generation of long-range ordered NPG structures is limited by the prior irregular interconnection of GNRs via a non-selective interribbon coupling. We note that, as recently demonstrated, these undesired reactions can be avoided by guiding the reaction with an interdigitated GNR template, thereby enabling the formation of an NPG with alternating undoped and N-doped GNRs.[47]

Our study reflects the relevance of molecular precursor design in the preservation of functional groups and the reduction of reaction steps, both key for the synthesis of heteroatom doped and functionalized graphene nanostructures, and demonstrates that a rational design can enable the generation of covalent supraribbon structures such as nanoporous graphene.

4. Experimental Section

Synthesis of the Molecular Precursors: A detailed description of the synthetic route for the preparation of each molecular precursor by means of solution chemistry could be found in the Supporting Information.

Sample Preparation: The Au(111) single crystal was prepared by repeated sputter-anneal cycles using Ar^+ ions at an energy of 1 keV and annealing to 470 °C. Precursors **3** and **4** were deposited at a rate of 0.013 monolayer/min and 0.005 monolayer/min respectively with the Au(111) held at room temperature, where the monolayer was referred to the saturated self-assembled layer of precursors. Both monomers were sublimated from the same commercial Dodecon OMBE fourfold Knudsen cell. The sample temperature was measured by using a thermocouple directly in contact with the sample. The base pressure during evaporation was below 1×10^{-9} mbar.

X-ray Photoelectron Spectroscopy: XPS spectra were acquired with a SPECS Phoibos 150 hemispherical energy analyzer using a monochromatic Al K_α X-ray source at 1486.6 eV. Measurements after each annealing step were carried out with the sample back at room temperature. XPS spectra were referenced to the Fermi level, fitted with a FermiDirac distribution at the sample temperature. The fitting results are summarized in Section S1.3 (Supporting Information).

Scanning Tunneling Microscopy and Spectroscopy: The topographic STM images were usually acquired in constant current (CC) mode and without any intentional functionalization of the tip apex. For intraribbon resolution, images were acquired in constant height (CH) mode, and with a CO-functionalized tip to perform bond-resolved STM (BR-STM). All conditions for image acquisition were summarized in Table S8 (Supporting Information). For the tip functionalization, CO molecules were first introduced on the Au surface by dosing the cryostat with CO gas at a pressure of 5×10^{-7} mbar for 30 s with the cryoshield doors of the STM open (temperature range from 5 to 15 K). In the STM images after CO dosing, CO molecules appear assemble in 2D clusters that nucleate at the elbows of the fcc sites of the Au(111) herringbone reconstruction. The tip was functionalized by a gentle indentation onto one of these CO clusters, or spontaneously by using a relatively small tip-sample distances (low voltages). Tip functionalization was recognized by a significant enhancement of the image resolution. The higher resolution of these tips were related to dynamic effects in the CO-metallic tip junction as it interacts with the atoms beneath.[56] dI/dV spectra of Figure 4 were acquired in CH mode, whereas the conductance maps were acquired in CC mode with a standard metallic tip using the lock-in technique. All the parameters are listed in Table S8 (Supporting Information).

DFT Calculations: All the electronic structure analysis in this work had been performed with DFT calculations using the SIESTA code.[57–59]. For the simulations the authors used the PBE form of the GGA exchange- correlation functional, with an optimized DZP basis set with diffuse orbitals for C and H atoms and the default DZP basis set for N with an energy shift of 0.01 Ry. The structures were relaxed up to a force tolerance of 0.01 eV $Å^{-1}$. To avoid interactions between periodic replicas of the 2D layer, a large vacuum region ≈35 nm was included in the simulation box. The mesh cut-off was set to 400 Ry. To sample the reciprocal space, they used a Monkhorst–Pack grid with 30 k points in the longitudinal (ribbon) direction and at least 3 k points in the transversal direction. Post processing of the results was done using the sisl python package.[60]

Supporting Information

Supporting Information is available from the Wiley Online Library or from the author.

Acknowledgements

The authors acknowledge Guillaume Sauthier for assisting us with the XPS experiments. This research was funded by the CERCA Programme/Generalitat de Catalunya and supported by Grant No. SEV-2017-0706 funded by the Spanish Ministry of Economy and Competitiveness (MINECO), Grant Nos. CEX2021-001214-S, PID2019-107338RB-C65, PID2019-107338RB-C62, and PGC2018-096955-B-C43 funded by MCIN/AEI /10.13039/501100011033, FLAG-ERA grant LEGOCHIP Projects PCI2019-111890-2 and PCI2019-111933-2 funded by MCIN/AEI /10.13039/501100011033 and cofounded by the European Union, Grant Nos. TED2021-132388B-C41 and TED2021-132388B-C42 funded by MCIN/AEI /10.13039/501100011033 and the European Union NextGenerationEU/ PRTR, the GenCat (Grant No. 2017SGR1506), the European Union MaX Center of Excellence (EU-H2020 Grant No. 924143), and Xunta de Galicia (Centro de Investigación de Galicia accreditation 2019–2022, ED431G 2019/03, and Oportunius Program). C.M. was supported by Grant RYC2019-028110-I funded by MICIN/AEI/10.13039/501100011033 and by the European Social Fund "ESF Investing in your future". M.T. was supported by Spanish State Research Agency/FSE (ref. BES-2017-08078, project ref. SEV-2013-0295-17-2). The authors thankfully acknowledge the computer resources at MareNostrum and the technical support provided by Barcelona Supercomputing Center (RES-QCM-2019-1-0051).

Conflict of Interest

The authors declare no conflict of interest.

Data Availability Statement

The data that support the findings of this study are available from the corresponding author upon reasonable request.

Keywords

graphene nanoribbons, heteroatom doping, nanoporous graphene, on-surface syntheses, scanning tunneling microscopy, X-ray photoelectron spectroscopy

Received: August 1, 2023
Published online:

[1] X. Wang, X. Li, L. Zhang, Y. Yoon, P. K. Weber, H. Wang, J. Guo, H. Dai, *Science* **2009**, *324*, 768.
[2] C. Bronner, S. Stremlau, M. Gille, F. Braußе, A. Haase, S. Hecht, P. Tegeder, *Angew. Chem., Int. Ed.* **2013**, *52*, 4422.
[3] H. Kim, K. Lee, S. I. Woo, Y. Jung, *Phys. Chem. Chem. Phys.* **2011**, *13*, 17505.
[4] M. Liu, Y. Song, S. He, W. W. Tjiu, J. Pan, Y. Y. Xia, T. Liu, *ACS Appl. Mater. Interfaces* **2014**, *6*, 4214.
[5] X. Hou, Q. Hu, P. Zhang, J. Mi, *Chem. Phys. Lett.* **2016**, *663*, 123.
[6] A. Yadegari, L. Samiee, S. Tasharrofi, S. Tajik, A. Rashidi, F. Shoghi, M. Rasoulianboroujeni, M. Tahriri, S. J. Rowley-Neale, C. E. Banks, *RSC Adv.* **2017**, *7*, 55555.
[7] Y. Bian, H. Wang, J. Hu, B. Liu, D. Liu, L. Dai, *Carbon* **2020**, *162*, 66.
[8] C. Bie, H. Yu, B. Cheng, W. Ho, J. Fan, J. Yu, *Adv. Mater.* **2021**, *33*, 1.
[9] E. F. Holby, C. D. Taylor, *Appl. Phys. Lett.* **2012**, *101*, 1.
[10] Z. Liang, D. Yang, P. Tang, C. Zhang, J. Jacas Biendicho, Y. Zhang, J. Llorca, X. Wang, J. Li, M. Heggen, J. David, R. E. Dunin-Borkowski, Y. Zhou, J. R. Morante, A. Cabot, J. Arbiol, *Adv. Energy Mater.* **2021**, *11*, 5.
[11] J. Amaro-Gahete, A. M. Kaczmarek, D. Esquivel, C. Jiménez-Sanchidrián, P. Van Der Voort, F. J. Romero-Salguero, *Chem. - Eur. J.* **2019**, *25*, 6823.
[12] D.-e. Jiang, V. R. Cooper, S. Dai, *Nano Lett.* **2009**, *9*, 12.
[13] O. S. Kwon, S. J. Park, J. Y. Hong, A. R. Han, J. S. Lee, J. S. Lee, J. H. Oh, J. Jang, *ACS Nano* **2012**, *6*, 1486.

[14] Q. Chen, X. Yang, *J. Membr. Sci.* **2015**, *496*, 108.
[15] H. Tan, X. Zhang, Z. Li, Q. Liang, J. Wu, Y. Yuan, S. Cao, J. Chen, J. Liu, H. Qiu, *iScience* **2021**, *24*, 1.
[16] H. W. Lee, H. S. Moon, J. Hur, I. T. Kim, M. S. Park, J. M. Yun, K. H. Kim, S. G. Lee, *Carbon* **2017**, *119*, 492.
[17] P. Lazar, R. Mach, M. Otyepka, *J. Phys. Chem. C* **2019**, *123*, 10695.
[18] Y. Yamada, H. Tanaka, S. Kubo, S. Sato, *Carbon* **2021**, *185*, 342.
[19] W. Zhao, O. Höfert, K. Gotterbarm, J. Zhu, C. Papp, H.-P. Steinrück, *J. Phys. Chem. C* **2012**, *116*, 5062.
[20] J. Yang, X. Zhou, D. Wu, X. Zhao, Z. Zhou, *Adv. Mater.* **2017**, *29*, 1.
[21] P. Błoński, J. Tuček, Z. Sofer, V. Mazánek, M. Petr, M. Pumera, M. Otyepka, R. Zboil, *J. Am. Chem. Soc.* **2017**, *139*, 3171.
[22] S. Clair, D. G. de Oteyza, *Chem. Rev.* **2019**, *119*, 4717.
[23] Y. Zhang, Y. Zhang, G. Li, J. Lu, X. Lin, S. Du, R. Berger, X. Feng, K. Müllen, H. J. Gao, *Appl. Phys. Lett.* **2014**, *105*, 2.
[24] T. H. Vo, U. G. E. Perera, M. Shekhirev, M. Mehdi Pour, D. A. Kunkel, H. Lu, A. Gruverman, E. Sutter, M. Cotlet, D. Nykypanchuk, P. Zahl, A. Enders, A. Sinitskii, P. Sutter, *Nano Lett.* **2015**, *15*, 5770.
[25] T. Marangoni, D. Haberer, D. J. Rizzo, R. R. Cloke, F. R. Fischer, *Chem. - Eur. J.* **2016**, *22*, 13037.
[26] R. E. Blackwell, F. Zhao, E. Brooks, J. Zhu, I. Piskun, S. Wang, A. Delgado, Y.-L. Lee, S. G. Louie, F. R. Fischer, *Nature* **2021**, *600*, 647.
[27] P. Spijker, S. Kawai, S. Saito, A. S. Foster, E. Meyer, S. Osumi, S. Yamaguchi, *Nat. Commun.* **2015**, *6*, 1.
[28] R. R. Cloke, T. Marangoni, G. D. Nguyen, T. Joshi, D. J. Rizzo, C. Bronner, T. Cao, S. G. Louie, M. F. Crommie, F. R. Fischer, *J. Am. Chem. Soc.* **2015**, *137*, 8872.
[29] G. D. Nguyen, F. M. Toma, T. Cao, Z. Pedramrazi, C. Chen, D. J. Rizzo, T. Joshi, C. Bronner, Y. C. Chen, M. Favaro, S. G. Louie, F. R. Fischer, M. F. Crommie, *J. Phys. Chem. C* **2016**, *120*, 2684.
[30] J. Li, P. Brandimarte, M. Vilas-Varela, N. Merino-Díez, C. Moreno, A. Mugarza, J. S. Mollejo, D. Sánchez-Portal, D. Garcia De Oteyza, M. Corso, A. Garcia-Lekue, D. Peña, J. I. Pascual, *ACS Nano* **2020**, *14*, 1895.
[31] M. Panighel, S. Quiroga, P. Brandimarte, C. Moreno, A. Garcia-Lekue, D. Rey, G. Sauthier, G. Ceballos, D. Peña, A. Mugarza, *ACS Nano* **2020**, *14*, 11120.
[32] L. Talirz, P. Ruffieux, R. Fasel, *Adv. Mater.* **2016**, *28*, 6222.
[33] Y. F. Zhang, Y. Zhang, G. Li, J. Lu, Y. Que, H. Chen, R. Berger, X. Feng, K. Müllen, X. Lin, Y. Y. Zhang, S. Du, S. T. Pantelides, H. J. Gao, *Nano Res.* **2017**, *10*, 3377.
[34] M. Ohtomo, H. Hayashi, K. Hayashi, H. Jippo, J. Zhu, R. Hayashi, J. Yamaguchi, M. Ohfuchi, H. Yamada, S. Sato, *ChemPhysChem* **2019**, *20*, 3366.
[35] C. Moreno, M. Vilas-Varela, B. Kretz, A. Garcia-Lekue, M. V. Costache, M. Paradinas, M. Panighel, G. Ceballos, S. O. Valenzuela, D. Peña, A. Mugarza, *Science* **2018**, *360*, 199.
[36] C. Moreno, M. Panighel, M. Vilas-Varela, G. Sauthier, M. Tenorio, G. Ceballos, D. Peña, A. Mugarza, *Chem. Mater.* **2019**, *31*, 331.
[37] C. Moreno, M. Paradinas, M. Vilas-Varela, M. Panighel, G. Ceballos, D. Peña, A. Mugarza, *Chem. Commun.* **2018**, *54*, 9402.
[38] J. Cai, P. Ruffieux, R. Jaafar, M. Bieri, T. Braun, S. Blankenburg, M. Muoth, A. P. Seitsonen, M. Saleh, X. Feng, K. Müllen, R. Fasel, *Nature* **2010**, *466*, 470.
[39] G. Gabka, P. Bujak, K. Giedyk, K. Kotwica, A. Ostrowski, K. Malinowska, W. Lisowski, J. W. Sobczak, A. Pron, *Phys. Chem. Chem. Phys.* **2014**, *16*, 23082.
[40] R. Hatada, S. Flege, W. Ensinger, S. Hesse, S. Tanabe, Y. Nishimura, K. Baba, *Coatings* **2020**, *10*, 1.
[41] A. Batra, D. Cvetko, G. Kladnik, O. Adak, C. Cardoso, A. Ferretti, D. Prezzi, E. Molinari, A. Morgante, L. Venkataraman, *Chem. Sci.* **2014**, *5*, 4419.
[42] C. Bronner, J. Björk, P. Tegeder, *J. Phys. Chem. C* **2015**, *119*, 486.
[43] M. Abyazisani, J. M. MacLeod, J. Lipton-Duffin, *ACS Nano* **2019**, *13*, 9270.
[44] H. Söde, L. Talirz, O. Gröning, C. A. Pignedoli, R. Berger, X. Feng, K. Müllen, R. Fasel, P. Ruffieux, *Phys. Rev. B- Condens. Matter Mater. Phys.* **2015**, *91*, 1.
[45] R. Pawlak, X. Liu, S. Ninova, P. D'Astolfo, C. Drechsel, S. Sangtarash, R. Häner, S. Decurtins, H. Sadeghi, C. J. Lambert, U. Aschauer, S. X. Liu, E. Meyer, *J. Am. Chem. Soc.* **2020**, *142*, 12568.
[46] J. Cai, C. A. Pignedoli, L. Talirz, P. Ruffieux, H. Söde, L. Liang, V. Meunier, R. Berger, R. Li, X. Feng, K. Müllen, R. Fasel, *Nat. Nanotechnol.* **2014**, *9*, 896.
[47] M. Tenorio, C. Moreno, P. Febrer, J. Castro-Esteban, P. Ordejón, D. Peña, M. Pruneda, A. Mugarza, *Adv. Mater.* **2022**, *34*, 2110099.
[48] L. E. Dinca, C. Fu, J. M. MacLeod, J. Lipton-Duffin, J. L. Brusso, C. E. Szakacs, D. Ma, D. F. Perepichka, F. Rosei, *ACS Nano* **2013**, *7*, 1652.
[49] P. H. Jacobse, A. van den Hoogenband, M. E. Moret, R. J. Klein Gebbink, I. Swart, *Angew. Chem., Int. Ed.* **2016**, *55*, 13052.
[50] P. H. Jacobse, K. A. Simonov, M. J. Mangnus, G. I. Svirskiy, A. V. Generalov, A. S. Vinogradov, A. Sandell, N. Mårtensson, A. B. Preobrajenski, I. Swart, *J. Phys. Chem. C* **2019**, *123*, 8892.
[51] M. R. Ajayakumar, C. Moreno, I. Alcón, F. Illas, C. Rovira, J. Veciana, S. T. Bromley, A. Mugarza, M. Mas-Torrent, *J. Phys. Chem. Lett.* **2020**, *11*, 3897.
[52] F. Hanke, J. Björk, *Phys. Rev. B- Condens. Matter Mater. Phys.* **2013**, *87*, 1.
[53] W. Gao, T. A. Baker, L. Zhou, D. S. Pinnaduwage, E. Kaxiras, C. M. Friend, *J. Am. Chem. Soc.* **2008**, *130*, 3560.
[54] R. Zuzak, P. Brandimarte, P. Olszowski, I. Izydorczyk, M. Markoulides, B. Such, M. Kolmer, M. Szymonski, A. Garcia-Lekue, D. Sánchez-Portal, A. Gourdon, S. Godlewski, *J. Phys. Chem. Lett.* **2020**, *11*, 10290.
[55] A. Mairena, M. Baljozovic, M. Kawecki, K. Grenader, M. Wienke, K. Martin, L. Bernard, N. Avarvari, A. Terfort, K.-H. Ernst, C. Wäckerlin, *Chem. Sci.* **2019**, *10*, 2998.
[56] P. Jelinek, *J. Phys.: Condens. Matter* **2017**, *29*, 34.
[57] E. Artacho, E. Anglada, O. Diéguez, J. D. Gale, A. García, J. Junquera, R. M. Martin, P. Ordejón, J. M. Pruneda, D. Sánchez-Portal, J. M. Soler, *J. Phys.: Condens. Matter* **2008**, *20*, 6.
[58] A. García, N. Papior, A. Akhtar, E. Artacho, V. Blum, E. Bosoni, P. Brandimarte, M. Brandbyge, J. I. Cerdá, F. Corsetti, R. Cuadrado, V. Dikan, J. Ferrer, J. Gale, P. García-Fernández, V. M. García-Suárez, S. García, G. Huhs, S. Illera, R. Korytár, P. Koval, I. Lebedeva, L. Lin, P. López-Tarifa, S. G. Mayo, S. Mohr, P. Ordejón, A. Postnikov, Y. Pouillon, M. Pruneda, et al., *J. Chem. Phys.* **2020**, *152*, 204108.
[59] M. Soler, E. Artacho, J. D. Gale, A. Garc, J. Junquera, P. Ordej, S. Daniel, *J. Phys.: Condens. Matter* **2002**, *14*, 2745.
[60] N. Papior, sisl: v0.11.0, **2021**, https://doi.org/10.5281/zenodo.597181.

